Surface Lattice Plasmon Resonances by Direct In Situ Substrate Growth of Gold Nanoparticles in Ordered Arrays

Gail A. Vinnacombe-Willson, Ylli Conti, Steven J. Jonas, Paul S. Weiss, Agustín Mihi, and Leonardo Scarabelli*

Precise arrangements of plasmonic nanoparticles on substrates are important for designing optoelectronics, sensors and metamaterials with rational electronic, optical and magnetic properties. Bottom-up synthesis offers unmatched control over morphology and optical response of individual plasmonic building blocks. Usually, the incorporation of nanoparticles made by bottom-up wet chemistry starts from batch synthesis of colloids, which requires time-consuming and hard-to-scale steps like ligand exchange and self-assembly. Herein, an unconventional bottom-up wet-chemical synthetic approach for producing gold nanoparticle ordered arrays is developed. Water-processable hydroxypropyl cellulose stencils facilitate the patterning of a reductant chemical ink on which nanoparticle growth selectively occurs. Arrays exhibiting lattice plasmon resonances in the visible region and near infrared (quality factors of >20) are produced following a rapid synthetic step (<10 min), all without cleanroom fabrication, specialized equipment, or self-assembly, constituting a major step forward in establishing in situ growth approaches. Further, the technical capabilities of this method through modulation of the particle size, shape, and array spacings directly on the substrate are demonstrated. Ultimately, establishing a fundamental understanding of in situ growth has the potential to inform the fabrication of plasmonic materials; opening the door for in situ growth fabrication of waveguides, lasing platforms, and plasmonic sensors.

1. Introduction

For plasmonic nanoparticles, the resonant condition of collectively oscillating conduction electrons occurs at specific frequencies of light depending on the nanoparticle size, shape, material, and local dielectric environment.[1] This localized surface plasmon resonance (LSPR) effect can confine light in subwavelength volumes,[2] resulting in the generation of an enhanced electric field. However, these resonances are typically short lived, due to intrinsic high radiative optical losses that limit the associated quality factors (<10).[3] Nonetheless, arranging plasmonic nanoparticles into ordered arrays emerged as a convenient strategy to overcome this limitation and to boost the quality factors of the system. In this configuration the optical losses associated with LSPRs can be compensated under Bragg conditions by hybridization with the scattered waves in the plane of the array close to the position of the Rayleigh–Wood anomalies.[3] This compensation generates lattice plasmon resonances, and offers an additional possibility for tuning the optical properties, depending on the angle of illumination and the geometrical parameters of the array.[3] Due to their narrow bandwidth (<2 nm) and long lifetimes,[3–5] lattice plasmon resonances already impact the enhancement and manipulation of light–matter interactions,[6–8] sensing,[9–12] displays,[13] information storage[14] and anti-reflective materials.[15]

The development of a simple, scalable, and rapid technique that combines the benefits of top-down and bottom-up methods

G. A. Vinnacombe-Willson, P. S. Weiss
Department of Chemistry and Biochemistry
University of California, Los Angeles
Los Angeles, CA 90095, USA
Y. Conti, A. Mihi, L. Scarabelli
Institute of Materials Science of Barcelona
ICMAB-CSIC
Campus UAB
Bellaterra 08193, Spain
E-mail: lscarabelli@icmab.es

The ORCID identification number(s) for the author(s) of this article can be found under https://doi.org/10.1002/adma.202205330.

© 2022 The Authors. Advanced Materials published by Wiley-VCH GmbH. This is an open access article under the terms of the Creative Commons Attribution License, which permits use, distribution and reproduction in any medium, provided the original work is properly cited.

DOI: 10.1002/adma.202205330

S. J. Jonas, P. S. Weiss
California NanoSystems Institute
University of California, Los Angeles
Los Angeles, CA 90095, USA
S. J. Jonas
Department of Pediatrics
David Geffen School of Medicine
University of California, Los Angeles
Los Angeles, CA 90095, USA
P. S. Weiss
Department of Bioengineering
University of California, Los Angeles
Los Angeles, CA 90095, USA
P. S. Weiss
Department of Materials Science and Engineering
University of California, Los Angeles
Los Angeles, CA 90095, USA

**ADVANCED
SCIENCE NEWS**

www.advancedsciencenews.com

**ADVANCED
MATERIALS**

www.advmat.de

would improve access to finely tuned plasmonic ordered arrays tailored to desired applications.[16–18] As of now, top-down methods benefit from their control over the positions of the particles and the generalizability of the substrates,[5,6,19] where bottom-up approaches offer control over the surface chemistry and particle size and shape.[1,16,18–20] Capillary-assisted, electrophoretic, and templated self-assembly can be used to generate nanoparticle arrays from colloidal building blocks, offering affordable alternatives to top-down electron beam lithography, focused ion beam lithography, and electro- and thermal deposition.[18,20,21] Despite these advantages, beginning from colloidal suspensions often involves multistep, time-consuming processes that limit scalability. For instance, liters-scale batch pre-synthesis requires precise temperature and additional rate control and ligand exchange requires the addition of large excesses of capping ligands and multiple centrifugation steps.[18,22–24] Furthermore, the requirement of clean-room facilities, costly specialized equipment, and complex self-assembly steps present barriers preventing accessibility of plasmonic substrates.[25–27]

In situ growth is an unconventional approach where plasmonic structures are formed starting from inorganic precursors directly on the target substrate material without any initial colloidal synthesis steps.[28–32] The particles nucleate on the substrate, therefore, this process does not involve any batch synthesis, self-assembly, or ligand exchange, and time-consuming procedures can be circumvented. So far, the possibility to direct growth into tunable nanometric patterns has proven difficult to achieve via in situ growth.[31–35] Recent strategies for site-directed in situ gold nanoparticle growth include crack-templated reduction lithography and similar methods.[32,35] Despite the possibility of creating single-nanoparticle-wide features using these techniques, the patterns accessible are limited to lines with resolutions of microns to hundreds of nanometers. Chemical patterning via microcontact printing has been combined with in situ growth to grow gold nanoparticles selectively on tunable micron-scale features, but with limited control over the nanoparticle morphology.[33] Similar results were observed with in situ growth on top-down lithographically patterned chemical layers.[34] Block-copolymer micelle lithography represents a leading technique applying in situ growth, where addressable structures comprised of shape- and size-controlled plasmonic units are uniformly and reproducibly created with single-particle resolution.[36–38] However, standard block-copolymer micelle lithography is generally limited to array periodicities up to ≈300 nm, preventing access to lattice plasmon resonances in the visible and infrared.[36–39] Moreover, due to the reliance of the patterning on the assembly of block copolymer micelles, the arrays are typically constrained to hexagonal lattices and the casting process can take up to a few weeks (unless combined with additional top-down or soft-lithographic steps).[36–38] Current limitations of in situ growth methods include: i) controlling the particle morphology/uniformity, ii) fabricating easily modifiable patterns (and with good selectivity), and iii) producing arrays with sufficient quality to sustain lattice plasmon resonances. Ultimately, these barriers have reduced the popularity of in situ growth methods for the fabrication of plasmonic substrates compared to top-down nanofabrication (such as electron beam lithography) and/or the implementation of colloidally prepared nanoparticles. Furthermore,

a comprehensive mechanistic understanding of gold nanoparticle formation on substrates requires further study, and relatively little work has addressed fundamental synthetic aspects of in situ growth, especially compared to the body of work that has been developed for colloidal synthesis.

Here, we establish and demonstrate a straightforward in situ growth approach targeting tunable plasmonic lattices following a rapid bottom-up growth of gold nanoparticles onto chemically patterned reactive areas created by soft lithography. To fabricate these structures, water-soluble hydroxypropyl cellulose (HPC) sacrificial hole masks (or stencils), were applied to create patterned regions containing gold nanoparticle growth-active chemical ink. Subsequent site-selective growth of gold nanoparticles was performed with the addition of a droplet of growth solution onto the chemically patterned substrates in one rapid (<10 min), single synthetic step. We demonstrate that the composition of the growth solution can be modulated to alter the size and shape of the particles as they grow on the substrate. We apply a one-step direct surface growth to generate lattice plasmon resonances, showing that in situ growth techniques can be used for engineering plasmonic materials with low optical losses. The benefits of plasmonic nanoparticle patterning and direct engineering of lattice plasmon resonances by in situ growth can contribute to the development of more efficient quantitative chemical and biological sensors,[9–12] plasmonic catalytic substrates[40–42] and biomedical platforms,[43–46] offering far-reaching impacts in a broad range of fields.

2. Results and Discussion

2.1. Chemical Nanopatterning with Thermal Nanoimprint Lithography

Gold nanoparticle arrays were fabricated on polydimethylsiloxane (PDMS) substrates following the creation of nanometric chemical patterns following a scalable and versatile soft lithographic method. Specifically, water-processable HPC stencils were prepared via thermal nanoimprint lithography (t-NIL) as shown in **Figure 1**A and applied to direct gold nanoparticle growth to specific areas containing a strong chemical reductant.[47–50] Briefly, in the t-NIL process, aqueous solutions of HPC were spin-coated onto the substrate, then the film was placed in contact with a hard PDMS (hPDMS) mold. Pressure was applied to the mold (≈1 bar) as the substrate was heated above the HPC glass transition temperature (140 °C), generating patterned holes shaped by the mold (optimization of the applied pressure and substrate treatments are shown in Figure S2, Supporting Information). We demonstrate high-fidelity patterning of films ranging in height from tens to a few hundred nanometers (≈30–330 nm), by comparing the measured and simulated differential refraction spectra for HPC thin films prepared with identical procedures on silicon (Figure 1B, and Figure S3 and experimental details, Supporting Information). After t-NIL, the imprinted photonic structures confer iridescence to the patterned films, as shown in Figure 1C and Figure S3, Supporting Information. Successful array transfer was confirmed via scanning electron microscopy (SEM) in films as low as ≈30 nm (Figure 1D–F).
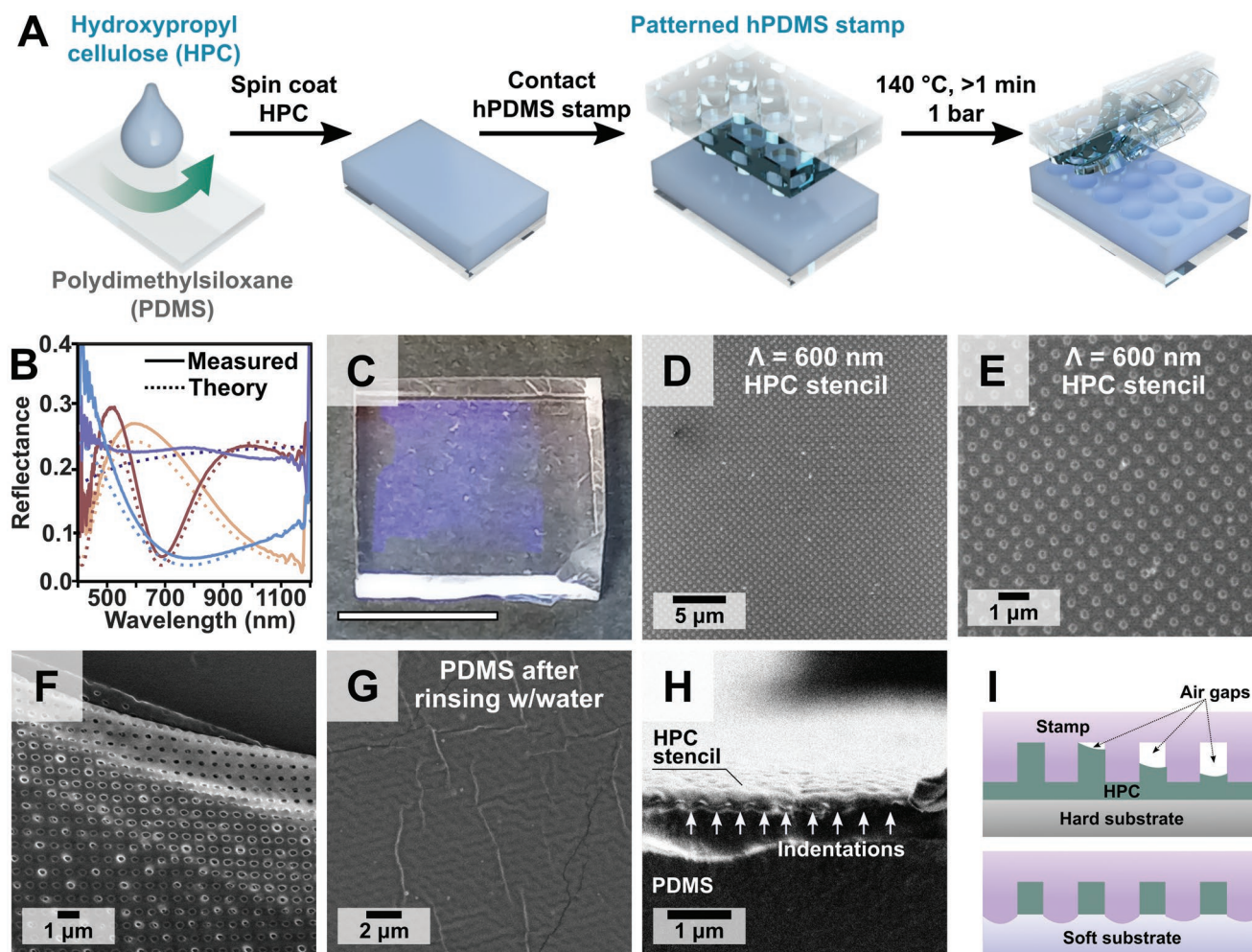
Figure 1. A) Schematic of hydroxypropyl cellulose (HPC) thermal nanoimprint lithography on poly(dimethylsiloxane) (PDMS). B) Reflectance spectra allowing the estimation of the film thickness on silicon: 30 nm (solid purple), 125 nm (solid blue), 192 nm (solid orange), and 330 nm (solid red) for the HPC aqueous solutions at different concentrations. The dotted lines represent the corresponding simulated interference generated by differential refraction for thin films with heights of 30 nm (dotted purple), 125 nm (dotted blue), 192 nm (dotted orange), and 330 nm (dotted red). C) Photograph of the ≈30 nm patterned HPC stencil with periodicities of 600 nm (Λ) resulting from the 21 mg mL^{-1} aqueous HPC solution (patterned area is 0.49 cm^2, scale bar: 0.7 cm). D–F) SEM images of different areas of the thinnest (30 nm) patterned HPC layer, with (F) showing a region at the edge of the film where holes are clearly visible. G) The PDMS substrate after removal of the HPC with water (indentation can be clearly observed), and H) the cross-section of a PDMS substrate with the imprinted HPC. I) Schematic showing imprinting of an HPC film with volume lower than the negative volume of the stamp on a hard (top) and soft (bottom) substrate. Details of sample preparation can be found in Scheme S3, Supporting Information.

This result seems counterintuitive, because normally with t-NIL, uniform patterns are not attainable with HPC volumes that do not match the negative volume of the stamp, which in our case corresponds to a film height of >250 nm (Scheme S6, Table S1, and calculations, Supporting Information). Electron microscopy analysis shows that the PDMS substrate is imprinted following the t-NIL process (Figure 1G,H). Therefore, we hypothesize that the key to patterning films nearly an order of magnitude lower in height than the normally required minimum is the implementation of the deformable receiving substrate, which helps to push the HPC into the vacant features as shown in Figure 1I.[25–27,51] This feature has important implications for the thickness of the residual layer. In standard t-NIL on rigid substrates, residual material remains in the imprinted features, usually measuring ca. 20 nm in height

for the patterns used here.[49,50] The removal of the excess material necessitates anisotropic reactive ion etching and cleanroom processing. Since we can pattern significantly thinner films, we estimate that the residual layer is accordingly greatly reduced (Figures S4 and S5, Supporting Information). Consequently, a quick (30 s) isotropic UV–ozone etch can effectively remove the excess HPC remaining in the holes. This etching step was successful for all HPC formulations that gave films with lower volume than the negative volume of the stamp (Figure S6, Supporting Information). Overall, the described procedure enables the reliable fabrication of HPC stencils with nanometric hole features (lattice parameter, Λ = 600 nm) without the use of any specialized or costly equipment or cleanroom fabrication. In addition, the same modified t-NIL technique can be extended from free-standing PDMS to glass-supported PDMS, improving
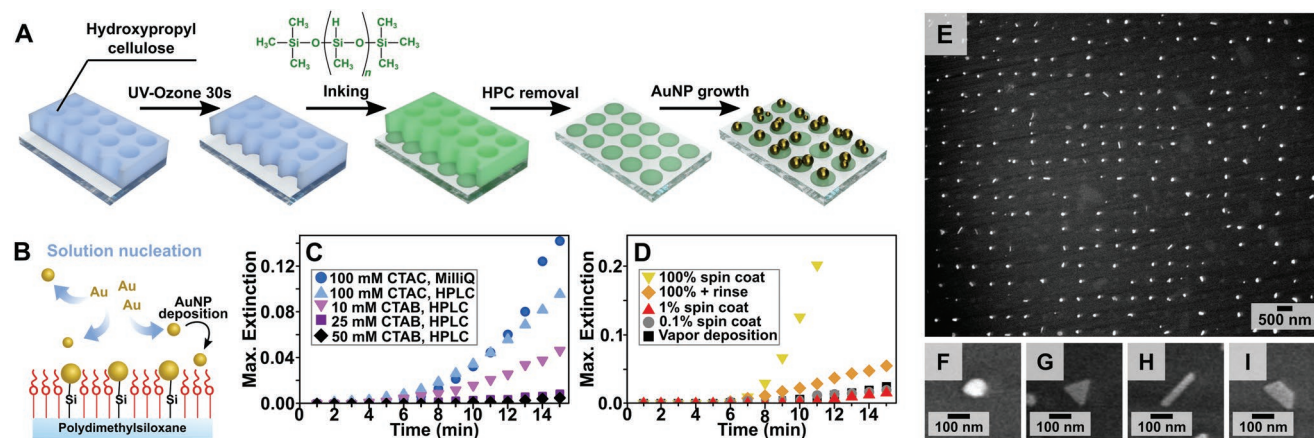
Figure 2. A) Schematic of the etching of the residual layer with UV–ozone, followed by inking with poly(methylhydrosiloxane), removal of the hydroxypropyl cellulose (HPC) with water, and introduction of the substrate into a growth solution to form gold nanoparticles (AuNPs). B) Schematic depicting competition between secondary solution nucleation and surface growth. C) Maximum extinction of growth solutions containing different water sources (Milli-Q or high-performance liquid chromatography, HPLC, water) and surfactant/capping ligand conditions (cetyltrimethylammonium bromide or chloride, CTAB/C, respectively), and all applying ascorbic acid as a mild reductant, over 15 min. D) Maximum extinction of growth solutions for substrates with different inking conditions. E) SEM image obtained under environmental conditions (60 Pa, low vacuum in water atmosphere) showing the patterned array after 10 min growth. F–I) SEM images showing a mixture of products suggesting different crystal structures and twinning: F) isotropic products, G) triangles, H) rods, and I) platelets/truncated triangles.

the ease of sample handling (Scheme S2, Figure S7, Materials and Methods, Supporting Information).

In the next step, the HPC stencils were used for the in situ growth of gold nanoparticles into ordered plasmonic arrays as shown in **Figure 2**A: following the 30 s UV–ozone etch, the polymethylhydrosiloxane chemical ink was applied on top of the stencil (Figure 2A). The integrity of the pattern of the HPC film is retained after the UV–ozone treatment and ink application steps as confirmed by SEM (Figure S4, Supporting Information). Then, the HPC stencil was dissolved in water, and the chemically patterned substrate was dried with an air gun. Finally, a fixed volume (150 µL) of gold nanoparticle growth solution containing surfactant cetyltrimethylammonium chloride or bromide as capping ligands, ascorbic acid as a mild reducing agent, and the gold inorganic precursor tetrachloroauric acid, $HAuCl_4$, was spread on the surface and was allowed to react for 10 min with the physisorbed ink (see the In Situ Gold Nanoparticle Growth section and Scheme S4, Supporting Information, for more details on the procedure and detailed composition of the solution). Following optimization, patterned particle growth into patterned arrays (≈0.5 mm² area) was confirmed by SEM (Figure 2B). The grown particles are mechanically stable and remain on the substrate after thorough rinsing and drying steps.

Decreasing the competition between nuclei formation on the substrate and nucleation in the growth solution is critical for successful in situ growth into patterns and for fundamental in situ size- and shape-control.[29,30,52–55] In standard colloidal gold nanoparticle seed-mediated synthesis, the nucleation and growth steps are spatiotemporally separated to control the final particle morphology.[1,56] First, small gold nuclei (also known as seeds) are uniformly grown and later added to a separate solution where they grow in a controlled manner into desired sizes and geometries. The nucleation step normally incorporates a strong reductant such as sodium borohydride for the fast,

uniform formation of seeds from the gold precursor. The following growth step instead includes weaker reductants, such as ascorbic acid, capable of reducing Au^{III} to Au^{I}, but confining the final reduction to Au^0 to the seed surface, promoting controlled growth. The seed-mediated synthesis scheme ensures suppression of later secondary nucleation events from occurring in the growth solution that would negatively affect size distribution and shape yield.[1,57]

One of the most important aspects explored here is the limitation and control of secondary nucleation, which has proven to be a particularly difficult challenge for in situ growth systems.[46,53,54,58] Here, the strong reductant ink is applied only on the substrate to mimic the spatially selective nucleation and growth processes used in colloidal synthesis, while the mild reductant ascorbic acid is added to the growth medium to facilitate the first reduction step of the gold salt from Au^{III} to Au^{I}. Although in our in situ growth scheme, we are only providing strong reductants on the surface of the substrate, colloidal nanoparticles can still spontaneously form from the precursors in the growth solution. Thus, secondary nucleation for in situ systems can be described as the uncontrolled formation of nuclei away from sites explicitly containing the strong reductant, which contributes to irreproducible consumption of reagents and solution-deposited particles outside the pattern (Figure 2C).

Even though nucleation can be achieved with the sole use of the physisorbed ink, our motivation behind adding ascorbic acid is to reduce the growth time and use of lower concentrations of gold precursor.[30,59,60] In fact, using only a surface-bound strong reductant usually requires ≈5 times more gold salt and hours to days long incubation.[31,32,35] Continuing with the goal of limiting secondary nucleation, we identified factors that could lead to the undesired spontaneous formation of colloids: i) the presence of impurities in the growth solution, ii) growth rate, and iii) excess ink leeching into solution. Regarding impurities, the water source is known to

**ADVANCED
SCIENCE NEWS**

www.advancedsciencenews.com

**ADVANCED
MATERIALS**

www.advmat.de

play important roles in colloidal synthesis, especially for the synthesis of anisotropic particles.[61,62] Recent work shows that faster growth kinetics can favor colloidal nucleation over nucleation on the substrate.[54] Therefore, we modulated the rate of the reaction by changing the type and concentration of the surfactant (cetyltrimethylammonium chloride or bromide, CTAC or CTAB, respectively). Lastly, we tested different inking methods and ink concentrations. The appearance of LSPR peaks evaluated by ultraviolet–visible spectroscopy indicated the occurrence of secondary nucleation, and the maximum intensity of the peaks was monitored over 15 min to track the severity of unwanted nuclei formation under different growth conditions (Figure 2D,E, and Figure S8, Supporting Information). Overall, growth solutions containing high-performance liquid chromatography (HPLC) grade water, and $25–50 \times 10^{-3}$ M CTAB gave the least secondary nucleation (Figure 2D). This optimized growth formulation was fixed and the application of chemical ink via different routes was tested. Aside from vapor deposition, the least amount of secondary nucleation was observed when dilute (1% or 0.1%) solutions of the ink were spin-coated onto the substrate (Figure 2E). Spin coating dependably produced patterns, and all conditions appeared to give similar nucleation site densities (Figures S4, S9, and S10, Supporting Information). Therefore, the 0.1% solution was selected for the following sections. After 10 min of growth, the products appeared to have a different crystal structure and twinning, and isotropic products, triangles, rods and other platelets could be observed (Figure 2F–I). In the next section, we explore size and shape-modification of the products.

2.2. In Situ Size and Shape Modification

Although little prior work has addressed mechanistic aspects of substrate-grown particles,[53–55,63–66] fundamentals of in situ growth remain vastly unexplored compared to colloidal batch systems.[59] Limiting the growth-active areas to diameters of <100 nm has the potential to enable tighter control over both nucleation and growth conditions. Next, we demonstrate the capability to modulate the size and morphology of the synthesized particles by changing the growth medium constituents and parameters, following concepts derived from colloidal synthesis.

Nanoparticle size was controlled by tuning the growth times between 1 and 10 min using the optimized growth solution from Figure 2 containing cetyltrimethylammonium bromide as a capping ligand and ascorbic acid as the mild reductant (**Figure 3**A–D, see Materials and Methods, Supporting Information, section for details). After 1 min of growth, the average particle size reaches 40 ± 14 nm (Figure 3E), which is relatively fast compared to colloidal synthesis.[24,67,68] At 2 min, the products nearly double in size to 70 ± 30 nm (Figure 3F). Growth times of 5 and 10 min result in nanoparticles with similar diameters (120 ± 40 and 110 ± 40 nm, respectively, Figure 3G,H). This behavior is consistent with other in situ growth studies.[28,58,69,70] Another interesting aspect to consider is the shape distributions of the nanoparticles grown. In colloidal synthesis of gold nanospheres, mixtures of various anisotropic (elongated structures, platelets) and isotropic (multi-twinned objects, cubes, pyra-
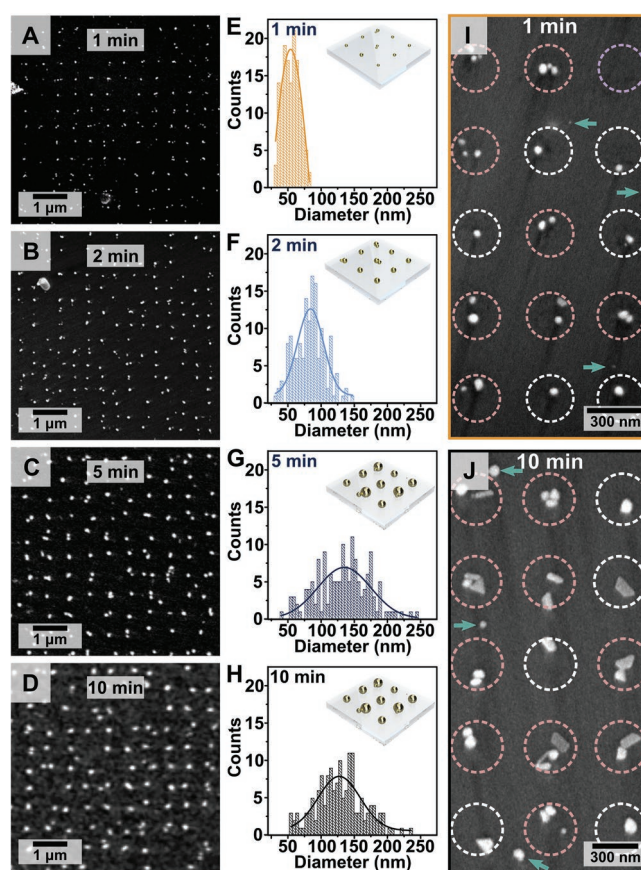

Figure 3. A–D) SEM images of patterned nanoparticle substrates after 1 min (A), 2 min (B), 5 min (C), and 10 min (D) growth with a growth solution containing cetyltrimethylammonium bromide (capping ligand/surfactant), gold salt, and ascorbic acid as a mild reducing agent. E–H) Size distributions for the 1 min (E), 2 min (F), 5 min (G), and 10 min (H) samples (150 nanoparticles each, $n = 10$). I,J) Representative SEM images showing pattern yield and common defects: multiple particles per area (pink circles), vacancies (purple circles), and particles outside the pattern (green areas). Patterned regions with single particles are indicated with a white circle ($n = 10$).

mids) products are obtained if no shape-control strategy is used during growth.[71–73] We observe similar behavior in the case of in situ grown particles. Even though the limitations of environmental SEM prevent us from distinguishing between different isotropic products (Figure 2F), we were able to identify platelets (Figure 2G,I) and rod-shaped geometries (Figure 2H), enabling us to evaluate their percentages and/or shape yield. Along with a change in the average nanoparticle diameter, shorter growth times were associated with lower percentages of total platelet and rod-shaped products. We estimate that the percentage of isotropic products decreased from ≈60% at 10 min to ≈90% at 1 min ($n = 150$ nanoparticles, Figure S11 and Table S2, Supporting Information). After 5 min, the nanoparticles formed at the specified nucleation sites no longer increase in size, possibly due to the onset of secondary nucleation effects. This hypothesis is supported by our evaluation of the patterning yield presented in Table S3, Supporting Information, where the percentage of particles outside the pattern slightly increases from 10% to 14% between 5 and 10 min.

Regarding patterning evaluation, various kinds of defects in the arrays are observed (Figure 3I,J). Standard defects include vacancies (purple circles), multiple particles per region (pink circles), and particles outside the patterned region (green arrows). The patterning yield was evaluated as the percentage of ink-containing regions that produced nanoparticles across all growth times as ≈80% (detailed evaluation summarized is in Figure S12 and Table S3, Supporting Information). The total percentage of nanoparticles located within the growth active regions was estimated to be ≈90%, indicating a strong preference for nucleation and growth within the pattern features due to the chemical contrast created by the presence and absence of the ink.

The identification of the sources of defects could assist in the future development of our in situ growth method; therefore, we next elaborate on this topic. Nanoparticles outside of the pattern (≈10% of all particles) result either from secondary homogeneous nucleation events in the growth solution (followed by particle deposition on the surface), non-specific spontaneous nucleation on regions without ink, or defects in the HPC mask. The appearance of vacancies in the electron microscopy images could be caused by resolution limitations of environmental SEM, which complicates imaging particles smaller than 2 nm. If instrument resolution was the primary cause of observed vacancies, one would expect these small nuclei to grow eventually into larger, more easily measurable nanoparticles. However, the percentage of vacancies remains constant when growth time is increased from 1 to 10 min; therefore, we infer that the vacancies do not contain nanoparticles. Another hypothesis to explain the vacancies can be related to defects in the HPC stencil, causing local removal of the ink during the washing step. The exploration of different chemical inks to increase the chemical contrast of the patterned regions and the substrate could be pursued in the future to reduce the abovementioned defects. Finally, both the presence of nanoparticles that are not centered in the patterned area and the growth of multiple particles in certain regions can arise from the size mismatch between the growing particles and the patterned features, with the latter being much larger (>270 nm). Nonetheless, the average number of nanoparticles per patterned area corresponds to 2 particles per circular region (not counting vacancies). This is an important observation because it suggests that once the initial nuclei are formed, their growth is favored over the later formation of new nuclei. The formation of new nuclei is disfavored due to the preference for continued growth on the already-formed nuclei and/or due to charge screening affecting the transport of gold salt to the substrate.[61,71] Moreover, this statistic gives us an estimate of the number of particles on each substrate as ≈2×10^8 particles/substrate, or ≈2×10^9 particles mL^{-1} of growth solution (assuming 100% yield of the t-NIL and ink patterning). The seed concentration in colloidal synthesis is usually 2–4 orders of magnitude higher (typical values for colloidal synthesis range between 10^{11} and 10^{13} seeds mL^{-1} of growth solution), giving us a much higher HAuCl$_4$ to nanoparticle ratio.[61,68] This difference provides an explanation for the speed of growth and offers possible improvements to target smaller nanoparticles and/or slower kinetics.

Next, we demonstrate generating anisotropic shapes directly on the substrate through post-modification and overgrowth of the arrays prepared after 5 min of growth. Previously, in situ overgrowth has been performed on colloidal assemblies to create unique geometries, such as Janus nanostructures, core–shell, hybrid and anisotropic/branched structures,[74,75] which enable control over the plasmonic near-field with applications for photothermal or sensing applications, for example.[12,46,76,77] Here, we target overgrowth of branched nanostars, which are attractive due to high localization of electromagnetic fields present at their sharp tips,[46,76,78] their high extinction in the near-infrared biological window, and their capability for thermoplasmonic heating.[46,79] The nanoparticle arrays were overgrown by subsequent incubation in a nanostar growth solution containing additional gold precursor and shape-directing reagents (silver nitrate, laurylsulfobetaine, hydrochloric acid, and ascorbic acid, **Figure 4**A). Similar to the first growth step, synthetic conditions were optimized to minimize secondary nucleation away from the substrate within the 5 min overgrowth time by lowering the pH of the growth medium, which limits the reducing strength of ascorbic acid.[46] Following the overgrowth step, the substrate exhibited a change in color from red to dark blue. The extinction spectra after 5 min of standard nanoparticle growth with the cetyltrimethylammonium bromide growth solution gives one dominant LSPR dip at 575 nm, and the samples following 5 min of nanostar overgrowth exhibit high extinction in the near infrared region at 985 nm, matching the expected plasmonic response Figure 4B.[46] The corresponding colloid recipe for the one used here generally results in three main products: spheres, and low and high aspect ratio nanostars.[46,76] However, electron microscopy characterization interestingly showed a high yield of one major, highly branched product (Figure 4C,D). The yield of the nanostar arrays over a larger area (measuring ca. 2000 μm^2) can be appreciated in Figure 4E. Altogether, the data presented in Figure 4 indicate that although certain concepts might transfer from colloidal to substrate growth (e.g., applying shape-directing reagents to promote anisotropic growth), important differences remain between the two environments that can significantly affect the shapes of the final products. The in situ surface growth strategy reported here represents an ideal platform for the exploration of such effects.[46]

2.3. Geometrical Tuning of the Array and Lattice Plasmon Resonance Characterization

Perhaps the most striking advantage of combining t-NIL and in situ growth resides in the preparation of ordered plasmonic arrays with arbitrary geometries, achieving control at the same time over both LSPRs and lattice plasmon resonances.[47–50] Although past and recent work proposed this possibility in relation to other in situ growth schemes, lattice plasmon resonances have not previously been demonstrated experimentally using only direct surface growth.[36–39] The spatial and geometrical constraints of the state-of-the-art methods prevent engineering lattice plasmon resonances (as well as more complex light–matter interactions),[80–82] limiting the application of in situ growth for the design of metasurfaces and intricate plasmonic systems. Our in situ growth approach overcomes two major barriers, namely the requirement for lengthy self-assembly steps and the flexibility in array periodicity by modifying the hPDMS
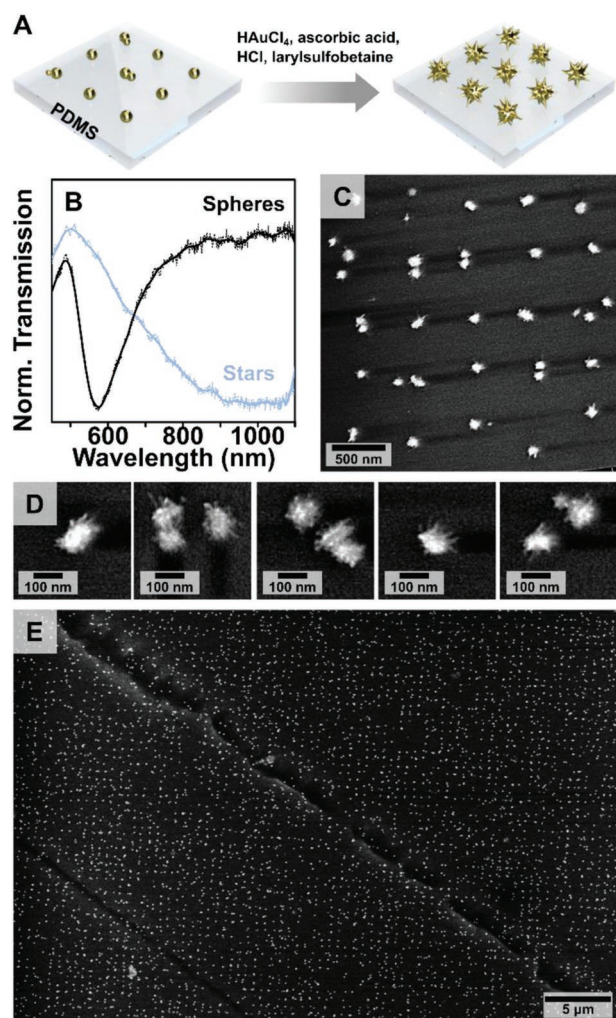
Figure 4. A) Schematic of overgrowth process into nanostars on poly(dimethylsiloxane) (PDMS). B) Normalized and smoothed (Savitzky–Golay) transmission spectra comparing the plasmon band position before (5 min growth in cetyltrimethylammonium bromide solution with ascorbic acid added as a weak reducing agent) and after stars overgrowth (5 min in a solution containing capping ligand/surfactant laurylsulfobetaine, HCl and ascorbic acid). C–E) SEM images of the nanostar arrays at different magnifications.

stamp.[50] Here, we measure lattice plasmon resonances for arrays with lattice parameters (Λ) of 400 and 500 nm, in addition to the Λ = 600 nm samples shown in Figures 1 and 3 (**Figure** 5A–F and Figures S13–S15, Supporting Information). Patterned in situ growth was achieved in all cases.

With the intention of maximizing the generation of lattice resonances through far-field coupling between the plasmonic units of the array, the particles were covered with a thin layer of soft PDMS after growth was complete. This step ensures a uniform refractive index environment around the plasmonic lattices, facilitating the propagation of the scattered field within the lattice plane.[3] Sharp lattice plasmon resonances were observed in the transmission profile under this refractive index matching condition (Figure 5G–J, sample preparation details are given in Scheme S5, Supporting Information) giving, to the best of our knowledge, the first demonstration of lattice

plasmon resonances via a purely in situ synthetic route, all without batch synthesis, self-assembly, top-down fabrication, nor costly and specialized equipment. Overall, this result shows that in situ growth can offer an inexpensive, simple, and rapid alternative for accessing collective plasmonic responses.

As expected, the wavelengths of the lattice plasmon resonances depend on the lattice parameter used for the preparation of the HPC masks (Figure 5G). Specifically, the most intense lattice plasmon resonances are expected to emerge in proximity to the first-order diffraction line, the spectral position of which can be predicted using the following simplified equation:[17]

$$\lambda = \Lambda_{x,y}(n \pm \sin\theta) \tag{1}$$

where $\Lambda_{x,y}$ represents the lattice parameters in the two orthogonal in plane directions, n is the refractive index of the surrounding medium, and θ is the illumination incidence angle. At normal incidence, where θ is defined as zero, for a square lattice where $x = y$, and with n_{PDMS} estimated to be 1.4, the predicted wavelengths can be calculated as: 560 nm for Λ = 400 nm, 700 nm for Λ = 500 nm, and 840 nm for Λ = 600 nm. In the 400 nm lattice parameter samples, the predicted lattice plasmon resonance overlaps with the LSPR of the gold nanoparticles and can be identified as a shoulder at 560 nm in the transmission spectrum. For the 500 nm lattice, a dip is observed at 698 nm, close to the predicted lattice plasmon resonance position. In the 600 nm lattice sample, the lattice plasmon resonance is observed at 826 nm (Figure 5G). The discrepancies compared to the predicted positions are common and can be attributed to factors including the effects of the CTAB gold nanoparticle coating, and/or the differences in PDMS refractive index as a function of composition and curing conditions.[21]

The identification of the aforementioned dips as lattice resonances is confirmed by measuring their spectral variation with illumination incidence angle (Figure 5H–J).[22] The dashed lines in Figure 5H–J are analytical calculations of the angular dependence of the Rayleigh–Wood anomalies. Apart from refractive index and lattice parameter, this dependence will also be modulated by the azimuthal angle of the array relative to the illumination (see discussion in Materials and Methods, Supporting Information). Additionally, the quality of the Λ = 600 nm array is also confirmed by the appearance of a second-order diffraction line (Figure 5J). Overall, the experimental data matched the predicted behavior, confirming the presence of lattice resonances.

Additionally, the quality of the observed lattice plasmon resonances was evaluated by calculating the quality factor (Q_F):

$$Q_F = \frac{\omega}{\Delta(\omega)} \tag{2}$$

where ω is the spectral peak position, and $\Delta(\omega)$ is the full width at half maximum of the peak. Using this relationship, we evaluate $Q_F = 29$ for Λ = 600 nm and $Q_F = 21$ for Λ = 500 nm. For the Λ = 400 nm array, we are unable to estimate the Q_F since the diffraction line is blue-shifted relative to the lattice resonance peak, producing an asymmetric Fano profile, as described in a prior publication[22] (details on Q_F calculations are in the optical characterization section, Supporting Information).
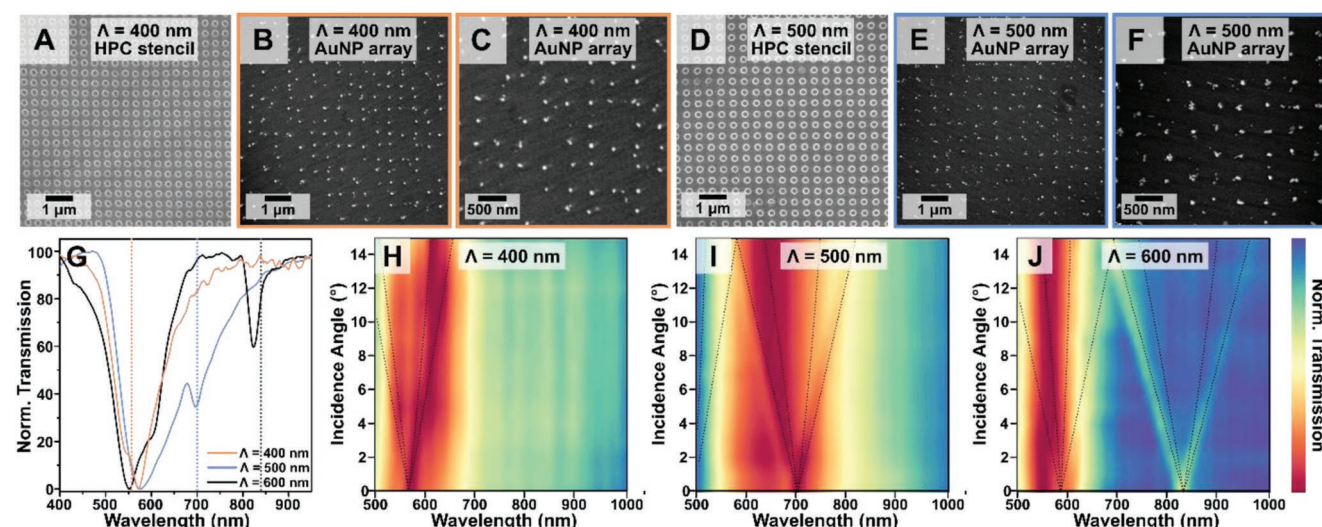
Figure 5. A–C) SEM images showing patterned hydroxypropyl cellulose (HPC) films with lattice parameter Λ = 400 nm (A) and the resulting patterned nanoparticle substrates (B,C). D–F) SEM images showing the Λ = 500 nm stencil (D) and the corresponding patterned nanoparticles (E,F) (SEM data for the Λ = 600 nm HPC stencils and resulting gold nanoparticle arrays are shown in Figures 1 and 3). G) Smoothed (Savitzky–Golay) and normalized transmission spectra of the substrates following refractive index matching. The dashed lines represent the theoretical position of Rayleigh–Wood anomalies (n_{PDMS} = 1.4). H–J) Contour plots showing measured angular dependence of the optical response optima for the Λ = 400 nm (H), Λ = 500 nm (I), and Λ = 600 nm (J) lattices. The dashed lines represent the predicted positions and displacement of the Rayleigh anomalies, depending on the azimuthal angle, using n_{PDMS} = 1.4. Additional SEM images can be found in Figures S13–S15, Supporting Information. All arrays were fabricated after 5 min of growth in the cetyltrimethylammonium bromide/ascorbic acid solution optimized from Figure 2 to limit secondary nucleation.

The Q_F for single-nanoparticle arrays prepared from colloidal suspensions typically fall within the range of Q_F = 10–30,[3,22,83] Thus, the performance of our arrays are on par with state-of-the-art methods based on single-particle assembly, despite the patterning defects and deviations in nanoparticle morphology that we observe. These results may be unexpected considering that our patterning yield is ≈80% (Figure 3I,J, and Figure S12 and Table S3, Supporting Information) and our shape-yield is ≈80–90% (Figure S11 and Table S2, Supporting Information), and any array defects would lead to broadening of the lattice resonance.[3,22,84] However, recent simulations by Manjavacas and co-workers suggest that by reducing the dimensions of the repeating unit below 100 nm, it is possible to achieve narrow LPRs, and that this effect is even more dramatic for realistic finite systems.[84] These observations lead us to hypothesize that the reduced dimensions of our in situ grown nanoparticles, and the absence of optical losses due to strong near-field coupling within the repeating unit (as for cluster plasmonic arrays), explain our observation of relatively sharp lattice resonances despite the presence of defects. Even though the fabricated arrays are less uniform than those prepared by state-of-the-art top-down[3,85] or colloidal synthesis/self-assembly approaches,[22,23] the demonstration of lattice plasmon resonances with bottom-up in situ substrate growth highlight its potential as a straightforward and easily accessible route for plasmonic materials engineering.

3. Conclusions and Prospects

A modified t-NIL protocol was used to pattern HPC thin films on soft polymeric substrates. This technique produced periodic structures with minimal residual layers such that water-processable sacrificial stencils can be created in a standard laboratory environment without special equipment. The sacrificial HPC masks were used for chemical patterning and subsequent site-selective bottom-up gold nanoparticle growth. The particle size and shape were controlled directly on the substrate by altering the growth time and growth media composition, respectively. The use of t-NIL provides improved flexibility for modifying the pattern increments over a wide range by changing the mask features without adjusting the patterning process or increasing the processing time. Following optimization of the chemical inking method and the nanoparticle growth solution, lattice plasmon resonances were demonstrated for arrays with periodicities of 400, 500 and 600 nm, giving tunable lattice plasmon resonances from the visible to the near infrared. The versatility in tuning the array geometry can be applied for potentially targeting lattice geometries giving collective responses beyond the near infrared, into the mid- or even far-infrared regions. The developed method overcomes limitations that have, until now, prevented the realization of lattice plasmon resonances using solely in situ growth, constituting significant progress for this class of approaches. Future work can target the fabrication of hybrid materials and superstructures with multiple synthetic steps, in order to engineer complex optical responses, like what has been achieved via metal nanoparticle–polymer systems.[86,87] The design and fabrication of sensors relying on surface-enhanced Raman spectroscopy can also be the target of future exploration,[29,30,65] especially since patterning can assist in controlling hot-spot density.[88]

Regarding fundamental synthetic aspects, understanding the roles of substrate wettability, particle–substrate interaction, secondary nucleation, the balance of reducing agents on the

substrate and in solution, effects of surface charge, chemical environment, and screening effects can help to create more reliable protocols achieving gold nanoparticle arrays and pave the way for new synthetic possibilities in the future.[39,89–91] Shape control for in situ-grown particles has only been briefly studied compared to colloidally synthesized particles and the need to probe various aspects of the growth thoroughly remains. In this regard, the in situ growth method presented here is versatile for future investigations studying wet-chemical shape control and selective surface growth. Furthermore, because the nanoparticles are fixed on the substrate, colloidal stability no longer represents a barrier to be considered, providing greater opportunities for testing unconventional growth conditions (e.g., surfactantless synthesis) or facile tailoring of the nanoparticle ligands. We anticipate that nanoparticle–substrate interactions will represent important aspects to explore, which can potentially be tuned via the selected metal,[92,93] selected ink, or the chosen substrate. The chosen substrate represents even more opportunities, that is, replacement of PDMS with different soft polymers,[94,95] conductive polymers,[96,97] hydrogels[98] and 2D materials.[99,100] In addition, the physical or chemical properties of the substrate could potentially be used as templates to facilitate the rotational order of products.[101,102] Ultimately, the presented methodology can bring a new perspective for the development of innovative synthetic paradigms for the growth of plasmonic nanoparticles and can impact the fabrication of solid-state platforms that take full advantage of the catalytic, optical, and magnetic properties of plasmonic nanoparticles.

Supporting Information

Supporting Information is available from the Wiley Online Library or from the author.

Conflict of Interest

The authors declare no conflict of interest.

Author Contributions

Experiments were designed by G.A.V.W. and L.S. Data were collected by G.A.V.W., L.S., and Y.C. G.A.V.W. and L.S. led the optimization of the HPC stencil fabrication. G.A.V.W., L.S., and Y.C. performed the synthesis optimization of the AuNPs into arrays. Morphological characterization of the AuNPs was performed by G.A.V.W. and L.S. Optical characterization was carried out by L.S. and Y.C. The manuscript was written by G.A.V.W., L.S., S.J.J., P.S.W., and A.M., with assistance from all other authors. All authors have given approval to the final version of the manuscript.

Data Availability Statement

The data that support the findings of this study are available from the corresponding author upon reasonable request.

[1] L. Liz-Marzán, *Colloidal Synthesis of Plasmonic Nanometals*, CRC Press, Boca Raton, FL, USA **2020**.

[2] K. A. Willets, R. P. Van Duyne, *Annu. Rev. Phys. Chem.* **2007**, *58*, 267.

[3] V. G. Kravets, A. V. Kabashin, W. L. Barnes, A. N. Grigorenko, *Chem. Rev.* **2018**, *118*, 5912.

[4] R. Adato, A. A. Yanik, C.-H. Wu, G. Shvets, H. Altug, *Opt. Express* **2010**, *18*, 4526.

[5] D. Wang, A. Yang, A. J. Hryn, G. C. Schatz, T. W. Odom, *ACS Photonics* **2015**, *2*, 1789.

[6] W. Zhou, M. Dridi, J. Y. Suh, C. H. Kim, D. T. Co, M. R. Wasielewski, G. C. Schatz, T. W. Odom, *Nat. Nanotechnol.* **2013**, *8*, 506.

[7] A. M. Berghuis, V. Serpenti, M. Ramezani, S. Wang, J. G. Rivas, *J. Phys. Chem. C* **2020**, *124*, 12030.

[8] T. S. Heiderscheit, S. Oikawa, S. Sanders, H. Minamimoto, E. K. Searles, C. F. Landes, K. Murakoshi, A. Manjavacas, S. Link, *J. Phys. Chem. Lett.* **2021**, *12*, 2516.

[9] C. Matricardi, C. Hanske, J. L. Garcia-Pomar, J. Langer, A. Mihi, L. M. Liz-Marzán, *ACS Nano* **2018**, *12*, 8531.

[10] D. G. Montjoy, J. H. Bahng, A. Eskafi, H. Hou, N. A. Kotov, *J. Am. Chem. Soc.* **2018**, *140*, 7835.

[11] G. Palermo, M. Rippa, Y. Conti, A. Vestri, R. Castagna, G. Fusco, E. Suffredini, J. Zhou, J. Zyss, A. De Luca, L. Petti, *ACS Appl. Mater. Interfaces* **2021**, *13*, 43715.

[12] E. Lenzi, D. Jimenez de Aberasturi, L. M. Liz-Marzán, *ACS Sens.* **2019**, *4*, 1126.

[13] J. Olson, A. Manjavacas, T. Basu, D. Huang, A. E. Schlather, B. Zheng, N. J. Halas, P. Nordlander, S. Link, *ACS Nano* **2016**, *10*, 1108.

[14] F. Yang, S. Ye, W. Dong, D. Zheng, Y. Xia, C. Yi, J. Tao, C. Sun, L. Zhang, L. Wang, Q. Chen, Y. Wang, Z. Nie, *Adv. Mater.* **2021**, *33*, 2100325.

2205330 (9 of 11)

[15] J. Jeon, K. Bhattarai, D.-K. Kim, J. O. Kim, A. Urbas, S. J. Lee, Z. Ku, J. Zhou, *Sci. Rep.* **2016**, *6*, 36190.

[16] M. A. Boles, M. Engel, D. V. Talapin, *Chem. Rev.* **2016**, *116*, 11220.

[17] S. Kasani, K. Curtin, N. Wu, *Nanophotonics* **2019**, *8*, 2065.

[18] L. Scarabelli, D. Vila-Liarte, A. Mihi, L. M. Liz-Marzán, *Acc. Mater. Res.* **2021**, *2*, 816.

[19] H. Zhang, C. Kinnear, P. Mulvaney, *Adv. Mater.* **2020**, *32*, 1904551.

[20] M. Mayer, M. Tebbe, C. Kuttner, M. J. Schnepf, T. A. F. König, A. Fery, *Faraday Discuss.* **2016**, *191*, 159.

[21] C. Rossner, T. A. F. König, A. Fery, *Adv. Opt. Mater.* **2021**, *9*, 2001869.

[22] P. Molet, N. Passarelli, L. A. Pérez, L. Scarabelli, A. Mihi, *Adv. Opt. Mater.* **2021**, *9*, 2100761.

[23] V. Gupta, P. T. Probst, F. R. Goßler, A. M. Steiner, J. Schubert, Y. Brasse, T. A. F. König, A. Fery, *ACS Appl. Mater. Interfaces* **2019**, *11*, 28189.

[24] N. Chiang, L. Scarabelli, G. A. Vinnacombe-Willson, L. A. Pérez, C. Dore, A. Mihi, S. J. Jonas, P. S. Weiss, *ACS Mater. Lett.* **2021**, *3*, 282.

[25] J. Dumond, H. Y. Low, *Adv. Mater.* **2008**, *20*, 1291.

[26] J. L. Perry, K. P. Herlihy, M. E. Napier, J. M. DeSimone, *Acc. Chem. Res.* **2011**, *44*, 990.

[27] T. Lee, C. Lee, D. K. Oh, T. Badloe, J. G. Ok, J. Rho, *Sensors* **2020**, *20*, 4108.

[28] F. Muench, S. Schaefer, L. Hagelüken, L. Molina-Luna, M. Duerrschnabel, H.-J. Kleebe, J. Brötz, A. Vaskevich, I. Rubinstein, W. Ensinger, *ACS Appl. Mater. Interfaces* **2017**, *9*, 31142.

[29] B. Fortuni, T. Inose, S. Uezono, S. Toyouchi, K. Umemoto, S. Sekine, Y. Fujita, M. Ricci, G. Lu, A. Masuhara, J. A. Hutchison, L. Latterini, H. Uji-i, *Chem. Commun.* **2017**, *53*, 11298.

[30] B. Fortuni, Y. Fujita, M. Ricci, T. Inose, R. Aubert, G. Lu, J. A. Hutchison, J. Hofkens, L. Latterini, H. Uji-i, *Chem. Commun.* **2017**, *53*, 5121.

[31] Q. Zhang, J.-J. Xu, Y. Liu, H.-Y. Chen, *Lab Chip* **2008**, *8*, 352.

[32] K. Park, M.-A. Woo, J.-A. Lim, Y.-R. Kim, S.-W. Choi, M.-C. Lim, *Colloids Surf., A* **2018**, *558*, 186.

[33] B. Wang, K. Chen, S. Jiang, F. Reincke, W. Tong, D. Wang, C. Gao, *Biomacromolecules* **2006**, *7*, 1203.

[34] A. A. Ellsworth, A. V. Walker, *Langmuir* **2016**, *32*, 2668.

[35] M.-C. Lim, S.-H. Kim, K. Park, Y.-R. Kim, J.-H. Kim, G. Ok, S.-W. Choi, *RSC Adv.* **2017**, *7*, 13228.

[36] M. Stefik, S. Guldin, S. Vignolini, U. Wiesner, U. Steiner, *Chem. Soc. Rev.* **2015**, *44*, 5076.

[37] T. Lohmüller, D. Aydin, M. Schwieder, C. Morhard, I. Louban, C. Pacholski, J. P. Spatz, *Biointerphases* **2011**, *6*, MR1.

[38] A. Alvarez-Fernandez, C. Cummins, M. Saba, U. Steiner, G. Fleury, V. Ponsinet, S. Guldin, *Adv. Opt. Mater.* **2021**, *9*, 2100175.

[39] H.-H. Jeong, M. C. Adams, J.-P. Günther, M. Alarcón-Correa, I. Kim, E. Choi, C. Miksch, A. F. Mark, A. G. Mark, P. Fischer, *ACS Nano* **2019**, *13*, 11453.

[40] L. Huang, P.-C. Chen, M. Liu, X. Fu, P. Gordiichuk, Y. Yu, C. Wolverton, Y. Kang, C. A. Mirkin, *Proc. Natl. Acad. Sci. USA* **2018**, *115*, 3764.

[41] E. Cortés, P. H. Camargo, *Plasmonic Catalysis: From Fundamentals to Applications*, John Wiley & Sons, New York **2021**.

[42] S. Ezendam, M. Herran, L. Nan, C. Gruber, Y. Kang, F. Gröbmeyer, R. Lin, J. Gargiulo, A. Sousa-Castillo, E. Cortés, *ACS Energy Lett.* **2022**, *7*, 778.

[43] Z. Ao, E. Parasido, S. Rawal, A. Williams, R. Schlegel, S. Liu, C. Albanese, R. J. Cote, A. Agarwal, R. H. Datar, *Lab Chip* **2015**, *15*, 4277.

[44] S.-W. Lv, Y. Liu, M. Xie, J. Wang, X.-W. Yan, Z. Li, W.-G. Dong, W.-H. Huang, *ACS Nano* **2016**, *10*, 6201.

[45] M.-H. Park, E. Reátegui, W. Li, S. N. Tessier, K. H. K. Wong, A. E. Jensen, V. Thapar, D. Ting, M. Toner, S. L. Stott, P. T. Hammond, *J. Am. Chem. Soc.* **2017**, *139*, 2741.

[46] G. A. Vinnacombe-Willson, N. Chiang, L. Scarabelli, Y. Hu, L. K. Heidenreich, X. Li, Y. Gong, D. T. Inouye, T. S. Fisher, P. S. Weiss, S. J. Jonas, *ACS Cent. Sci.* **2020**, *6*, 2105.

[47] M. Colburn, S. C. Johnson, M. D. Stewart, S. Damle, T. C. Bailey, B. Choi, M. Wedlake, T. B. Michaelson, S. V. Sreenivasan, J. G. Ekerdt, C. G. Willson, *Proc. SPIE* **1999**, https://doi.org/10.1117/12.351155.

[48] S. Y. Chou, P. R. Krauss, P. J. Renstrom, *J. Vac. Sci. Technol., B: Microelectron. Nanometer Struct.–Process., Meas., Phenom.* **1996**, *14*, 4129.

[49] A. Espinha, C. Dore, C. Matricardi, M. I. Alonso, A. R. Goñi, A. Mihi, *Nat. Photonics* **2018**, *12*, 343.

[50] C. Dore, J. Osmond, A. Mihi, *Nanoscale* **2018**, *10*, 17884.

[51] T. J. Merkel, K. P. Herlihy, J. Nunes, R. M. Orgel, J. P. Rolland, J. M. DeSimone, *Langmuir* **2010**, *26*, 13086.

[52] J. Tang, Q. Ou, H. Zhou, L. Qi, S. Man, *Nanomaterials* **2019**, *9*, 185.

[53] S. D. Golze, R. A. Hughes, S. Rouvimov, R. D. Neal, T. B. Demille, S. Neretina, *Nano Lett.* **2019**, *19*, 5653.

[54] T. B. Demille, R. A. Hughes, S. Neretina, *J. Phys. Chem. C* **2019**, *123*, 19879.

[55] S. Kumar, H. Yang, S. Zou, *J. Phys. Chem. C* **2007**, *111*, 12933.

[56] L. Scarabelli, *Pure Appl. Chem.* **2018**, *90*, 1393.

[57] N. G. Bastús, J. Comenge, V. Puntes, *Langmuir* **2011**, *27*, 11098.

[58] B. Landeke-Wilsmark, L. Nyholm, C. Hägglund, *Langmuir* **2020**, *36*, 6848.

[59] J. R. Dunklin, G. T. Forcherio, K. R. Berry, D. K. Roper, *J. Phys. Chem. C* **2014**, *118*, 7523.

[60] D. J. Campbell, R. B. Villarreal, T. J. Fitzjarrald, *J. Chem. Educ.* **2012**, *89*, 1312.

[61] L. Scarabelli, A. Sánchez-Iglesias, J. Pérez-Juste, L. M. Liz-Marzán, *J. Phys. Chem. Lett.* **2015**, *6*, 4270.

[62] L. M. Liz-Marzán, C. R. Kagan, J. E. Millstone, *ACS Nano* **2020**, *14*, 6359.

[63] T. B. Demille, R. A. Hughes, N. Dominique, J. E. Olson, S. Rouvimov, J. P. Camden, S. Neretina, *Nanoscale* **2020**, *12*, 16489.

[64] G. Liu, C. Zhang, J. Wu, C. A. Mirkin, *ACS Nano* **2015**, *9*, 12137.

[65] M. J. Ashley, M. R. Bourgeois, R. R. Murthy, C. R. Laramy, M. B. Ross, R. R. Naik, G. C. Schatz, C. A. Mirkin, *J. Phys. Chem. C* **2018**, *122*, 2307.

[66] C. Kuttner, V. Piotto, L. M. Liz-Marzán, *Chem. Mater.* **2021**, *33*, 8904.

[67] C. Hanske, G. González-Rubio, C. Hamon, P. Formentín, E. Modin, A. Chuvilin, A. Guerrero-Martínez, L. F. Marsal, L. M. Liz-Marzán, *J. Phys. Chem. C* **2017**, *121*, 10899.

[68] P. Chhour, J. Kim, B. Benardo, A. Tovar, S. Mian, H. I. Litt, V. A. Ferrari, D. P. Cormode, *Bioconjugate Chem.* **2017**, *28*, 260.

[69] Y. Sun, *Chem. Mater.* **2007**, *19*, 5845.

[70] T. Lohmueller, E. Bock, J. P. Spatz, *Adv. Mater.* **2008**, *20*, 2297.

[71] K. R. Brown, D. G. Walter, M. J. Natan, *Chem. Mater.* **2000**, *12*, 306.

[72] I. Pastoriza-Santos, L. M. Liz-Marzán, *Langmuir* **2002**, *18*, 2888.

[73] A. R. Tao, S. Habas, P. Yang, *Small* **2008**, *4*, 310.

[74] Q. Shi, D. E. Gómez, D. Dong, D. Sikdar, R. Fu, Y. Liu, Y. Zhao, D.-M. Smilgies, W. Cheng, *Adv. Mater.* **2019**, *31*, 1900989.

[75] Q. Cheng, L. Song, H. Lin, Y. Yang, Y. Huang, F. Su, T. Chen, *Langmuir* **2020**, *36*, 250.

[76] D. Jimenez de Aberasturi, A. B. Serrano-Montes, J. Langer, M. Henriksen-Lacey, W. J. Parak, L. M. Liz-Marzán, *Chem. Mater.* **2016**, *28*, 6779.

[77] J. J. Giner-Casares, M. Henriksen-Lacey, I. García, L. M. Liz-Marzán, *Angew. Chem., Int. Ed.* **2016**, *55*, 974.

**ADVANCED
SCIENCE NEWS**

www.advancedsciencenews.com

**ADVANCED
MATERIALS**

www.advmat.de

[78] E. Lenzi, D. Jimenez de Aberasturi, M. Henriksen-Lacey, P. Piñeiro, A. J. Muniz, J. Lahann, L. M. Liz-Marzán, *ACS Appl. Mater. Interfaces* **2022**, *14*, 20708.

[79] A. Casu, E. Cabrini, A. Donà, A. Falqui, Y. Diaz-Fernandez, C. Milanese, A. Taglietti, P. Pallavicini, *Chem. – Eur. J.* **2012**, *18*, 9381.

[80] J.-Y. Kim, J. Yeom, G. Zhao, H. Calcaterra, J. Munn, P. Zhang, N. Kotov, *J. Am. Chem. Soc.* **2019**, *141*, 11739.

[81] E. S. A. Goerlitzer, R. Mohammadi, S. Nechayev, K. Volk, M. Rey, P. Banzer, M. Karg, N. Vogel, *Adv. Mater.* **2020**, *32*, 2001330.

[82] P. T. Probst, M. Mayer, V. Gupta, A. M. Steiner, Z. Zhou, G. K. Auernhammer, T. A. F. König, A. Fery, *Nat. Mater.* **2021**, *20*, 1024.

[83] M. Juodėnas, T. Tamulevičius, J. Henzie, D. Erts, S. Tamulevičius, *ACS Nano* **2019**, *13*, 9038.

[84] A. Manjavacas, L. Zundel, S. Sanders, *ACS Nano* **2019**, *13*, 10682.

[85] Q. Le-Van, E. Zoethout, E.-J. Geluk, M. Ramezani, M. Berghuis, J. G. Rivas, *Adv. Opt. Mater.* **2019**, *7*, 1801451.

[86] K. Volk, T. Honold, D. Feller, M. Karg, *Adv. Mater. Interfaces* **2021**, *8*, 2100317.

[87] Y. Brasse, V. Gupta, H. C. T. Schollbach, M. Karg, T. A. F. König, A. Fery, *Adv. Mater. Interfaces* **2020**, *7*, 1901678.

[88] L. Osinkina, T. Lohmüller, F. Jäckel, J. Feldmann, *J. Phys. Chem. C* **2013**, *117*, 22198.

[89] A. G. Mark, J. G. Gibbs, T.-C. Lee, P. Fischer, *Nat. Mater.* **2013**, *12*, 802.

[90] G. Klös, M. Miola, D. S. Sutherland, *J. Phys. Chem. C* **2019**, *123*, 7347.

[91] G. Klös, A. Andersen, M. Miola, H. Birkedal, D. S. Sutherland, *Nano Res.* **2019**, *12*, 1635.

[92] B. Viswanath, P. Kundu, A. Halder, N. Ravishankar, *J. Phys. Chem. C* **2009**, *113*, 16866.

[93] Y. Shi, Z. Lyu, M. Zhao, R. Chen, Q. N. Nguyen, Y. Xia, *Chem. Rev.* **2021**, *121*, 649.

[94] E. S. Abdel-Halim, S. S. Al-Deyab, *Carbohydr. Polym.* **2011**, *86*, 1615.

[95] X. Wu, C. Lu, Z. Zhou, G. Yuan, R. Xiong, X. Zhang, *Environ. Sci.: Nano* **2014**, *1*, 71.

[96] Y.-C. Liu, T. C. Chuang, *J. Phys. Chem. B* **2003**, *107*, 12383.

[97] J. Han, L. Li, R. Guo, *Macromolecules* **2010**, *43*, 10636.

[98] C. Wang, N. T. Flynn, R. Langer, *Adv. Mater.* **2004**, *16*, 1074.

[99] J. Li, J. Xie, L. Gao, C. M. Li, *ACS Appl. Mater. Interfaces* **2015**, *7*, 2726.

[100] B. Song, K. He, Y. Yuan, S. Sharifi-Asl, M. Cheng, J. Lu, W. A. Saidi, R. Shahbazian-Yassar, *Nanoscale* **2018**, *10*, 15809.

[101] T. Jain, S. Lara-Avila, Y.-V. Kervennic, K. Moth-Poulsen, K. Nørgaard, S. Kubatkin, T. Bjørnholm, *ACS Nano* **2012**, *6*, 3861.

[102] A. J. Mieszawska, G. W. Slawinski, F. P. Zamborini, *J. Am. Chem. Soc.* **2006**, *128*, 5622.